AIAA JOURNAL
Vol. 41, No. 2, February 2003

Numerical Simulation: Supersonic Flow Around Wing–Body Configuration with Integrated Engine Nacelle

Masahiro Kanazaki,* Shigeru Obayashi,† and Kazuhiro Nakahashi‡
Tohoku University, Sendai 980-8577, Japan

A numerical simulation of flowfields around a supersonic transport aircraft with integrated engine nacelles is presented. In this study, flowfields were simulated by solving the Euler equations with the unstructured grid method for handling the complex geometry. To simulate intake flows at actual flight conditions, a throat was introduced inside the nacelle. The effect of nacelle mass flow ratios on overall aerodynamic performance was investigated in detail by changing throat heights. The spillage drag was calculated and found to have a large impact on the total drag. Computed results showed excellent agreement with wind-tunnel data obtained at the National Aerospace Laboratory of Japan.

Introduction

THE scaled supersonic experimental aircraft with propulsion system is now in the design stage at the National Aerospace Laboratory of Japan (NAL).[1] The preliminary configuration of the jet-powered experimental aircraft used for the wind-tunnel test is shown in Fig. 1. The design has to account for strong aerodynamic interactions among wings, fuselage, and nacelles.

The wind-tunnel model has flow-through nacelles. To simulate actual flights, nacelle mass flow ratios have to be controlled because the spillage drag is expected to have an influence on the airplane's total drag. Because it would be extremely difficult to control the nacelle mass flow by simulating the actual turbofan engine, a throat is introduced inside of the flow-through nacelle in this study. The nacelle mass flow ratios will be controlled by changing the height of the throat.

To handle the complex geometry of the wing–fuselage–nacelle configuration, the unstructured grid approach is employed.[2] The present grid generation process is streamlined so as to start from CAD data,[3] then to generate a surface grid,[4] and finally to generate a volume grid.[2,5] The three-dimensional Euler equations are employed for flow calculations.

The wind-tunnel model geometry of the jet-powered experimental model was designed at NAL using the CAD software CATIA. From the CATIA data provided by NAL, the unstructured surface grid was first generated by the advancing-front method. Various heights of throat shape are then introduced by deforming the boundary grid inside the nacelle. Several volume grids were generated corresponding to each throat height.

Aerodynamics performance of the wind-tunnel model will be calculated at various nacelle mass flow ratios and compared with experiment.[6] Typically, the aerodynamic forces are obtained by integrating pressures on the geometry surface. However, the spillage drag caused by the mass flow ratio variation into the nacelle controlled by the propulsion system can not be estimated by merely integrating pressures on the nacelle inner surface. Therefore, in this study, the spillage drag is estimated by the conservation of momentum to the inlet of the nacelle. Finally, to investigate the grid dependency of numerical solutions, calculations are performed by using fine and coarse grids.

Received 15 February 2002; revision received 26 October 2002; accepted for publication 26 October 2002.

*Graduate Student, Institute of Fluid Science.
†Associate Professor, Institute of Fluid Science. Associate Fellow AIAA.
‡Professor, Department of Aeronautics and Space Engineering. Associate Fellow AIAA.

Flow Solver

In this study, the flowfield was calculated by the Euler equations written as

$$\frac{\partial}{\partial t}\int_{\Omega} \boldsymbol{Q}\,\mathrm{d}V + \int_{\partial\Omega} \boldsymbol{F}(\boldsymbol{Q})\cdot\boldsymbol{n}\,\mathrm{d}S = 0 \tag{1}$$

where $\boldsymbol{Q} = [\rho, \rho u, \rho v, \rho w, e]^T$ is the vector of conservative variables; ρ is the density; u, v, and w are the Cartesian velocity components; and e is the total energy. The vectors $\boldsymbol{F}(\boldsymbol{Q})$ represent the inviscid flux and $\boldsymbol{n}$ is the outward normal of $\partial\Omega$, which is the boundary of the control volume Ω.

Equations (1) are solved by a finite volume cell-vertex scheme and can be written in algebraic form as follows:

$$\frac{\partial \boldsymbol{Q}_i}{\partial \boldsymbol{t}} = -\frac{1}{V_i}\left[\sum_{j(i)} \Delta S_{ij}\boldsymbol{F}(\boldsymbol{Q})_{ij}\cdot\boldsymbol{n}_{ij}\right] \tag{2}$$

where ΔS_{ij} is a segment area of the control volume boundary associated with the edge connecting points i and j. The term $\boldsymbol{F}$ is an inviscid numerical flux vector normal to the control volume boundary, and $Q_{ij}^{\pm}$ are values on both sides of the control volume boundary. The subscript of summation $j(i)$ refers to all node points connected to node i.

The Harten–Lax–van Leer–Einfeldt–Wada Riemann solver (see Ref. 7) is used for the numerical flux computations. Second-order spatial accuracy is realized by a linear reconstruction of the primitive variables $\boldsymbol{q} = [\rho, u, v, w, p]^T$ inside the control volume as

$$\boldsymbol{q}(x, y, z) = \boldsymbol{q}_i + \Psi_i \nabla \boldsymbol{q}_i \cdot (\boldsymbol{r} - \boldsymbol{r}_i) \tag{3}$$

where $\boldsymbol{r}$ is a position vector and i is the node number. The gradient associated with the control volume centroid is a volume-averaged gradient computed from the values in the surrounding grid cells. A numerical limiter Ψ is used to prevent overshoots of the interpolated solution during the flux computation. Here, Venkatakrishnan's limiter[8] is used because of its superior convergence properties.

The lower–upper symmetric Gauss–Seidel (LU-SGS) implicit method,[2] originally developed for a structured grid method, was applied earlier to compute the high-Reynolds-number flows efficiently. The LU-SGS method on the unstructured grid can be derived by splitting node points $j(i)$ into two groups, $j \in L(i)$ and $j \in U(i)$, for the first summation in the right-hand side of Eq. (2). With $\Delta\boldsymbol{Q} = \Delta\boldsymbol{Q}^{n+1} - \Delta\boldsymbol{Q}^{n}$, the final form of the LU-SGS method for the unstructured grid becomes two sweeps, including the forward sweep:

$$\Delta\boldsymbol{Q}_i^{*} = \boldsymbol{D}^{-1}\left[\boldsymbol{R}_i - \sum \Delta S_{ij}\boldsymbol{A}_j^{-}\Delta\boldsymbol{Q}_j^{*}\right] \tag{4a}$$

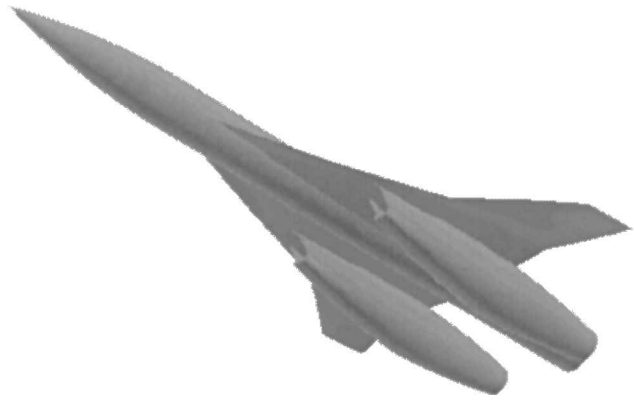

Fig. 1 Wind-tunnel model 01 for scaled supersonic experimental aircraft designed at NAL.

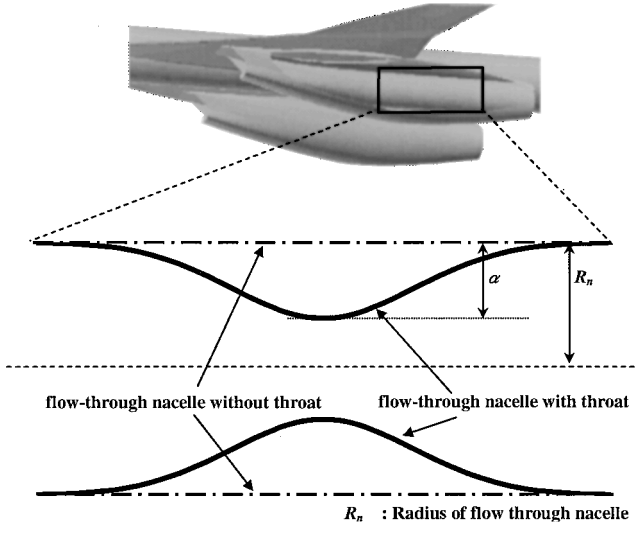

Fig. 2 Definition of throat shape by exponential function.

and the backward sweep:

$$\Delta \boldsymbol{Q}_i = \Delta \boldsymbol{Q}_i^* - \boldsymbol{D}^{-1} \sum_{j(i)} \Delta S_{ij} \boldsymbol{A}_j^- \Delta \boldsymbol{Q}_j \tag{4b}$$

where,

$$\boldsymbol{D} = \frac{V_i}{\Delta t} \boldsymbol{I} + \sum_{j(i)} \Delta S_{ij} \boldsymbol{A}_i^+ \tag{5}$$

The term $\boldsymbol{D}$ is diagonalized by the Jameson–Turkel approximation[9] of the Jacobian as $\boldsymbol{A}^{\pm} = 0.5(\boldsymbol{A} \pm \rho_A \boldsymbol{I})$, where ρ_A is a spectral radius of Jacobian $\boldsymbol{A}$. The lower–upper splitting of Eqs. (4) for the unstructured grid is done by a grid reordering technique[2] that was developed to improve the convergence and the vectorization.

Nacelle Mass Flow Control by Height of Throat Shape

Throat Shape Definition

The throat is introduced in the engine nacelle to examine the influence of nacelle mass flow ratios on the total aircraft drag (Fig. 2).

The throat shape is defined by an exponential function as

$$f_{\text{throat}} = \alpha \times \exp(-\beta \times x^2) \tag{6}$$

where α is a height of the throat and β is an indicator of the width of the throat. The height and width are normalized by the length of the fuselage. In this study, β is fixed at 0.095. The throat is placed in the nacelle by moving the surface grid as shown in Fig. 3.

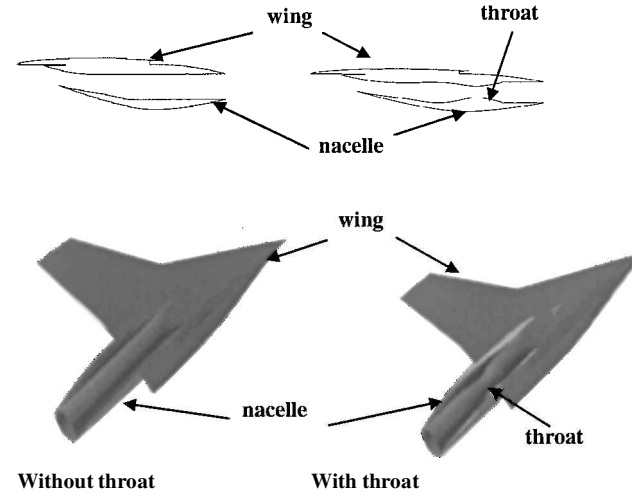

Fig. 3 Geometry of throat inside nacelle and cross-sectional view of nacelle.

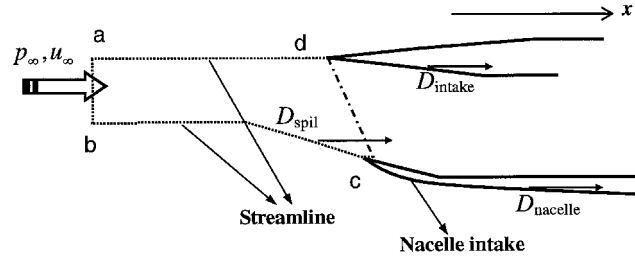

Fig. 4 Nacelle intake flow and streamlines.

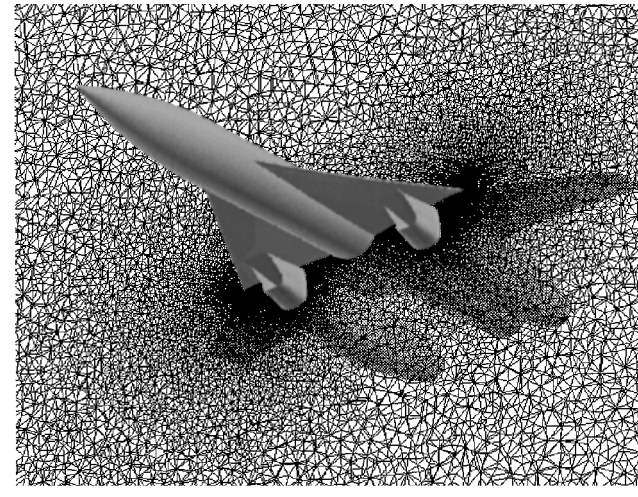

Fig. 5 Computational grid around the NAL scaled supersonic airplane medel.

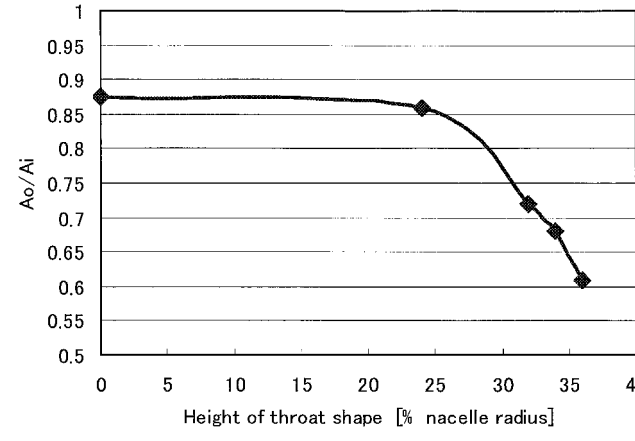

Fig. 6 Variation of mass flow ratios according to throat heights.

Nacelle Mass Flow Control

The nacelle mass flow ratios can be controlled by changing the height of throat. The mass flow into the nacelle $\dot{m}$ is written as

$$\dot{m} = \rho_e U_e A_e \tag{7}$$

where ρ_e, U_e, and A_e are density, velocity, and area at the exit of the nacelle, respectively. The mass flow $\dot{m}$ is normalized by the maximum mass flow into the nacelle $\dot{m}_{\max}$. The maximum mass flow $\dot{m}_{\max}$ is written as

$$\dot{m}_{\max} = \rho_\infty U_\infty A_i \tag{8}$$

where ρ_∞ and U_∞ are freestream density and velocity, respectively, and A_i is the intake area projected to the front view of the nacelle. Then the nacelle mass flow ratio can be written as

$$\frac{\dot{m}}{\dot{m}_{\max}} = \frac{\rho_e U_e A_e}{\rho_\infty U_\infty A_i} \tag{9}$$

Prediction of Spillage Drag

When the nacelle mass flow is controlled, the spillage drag should be calculated. The spillage drag can be predicted by the conservation of momentum,[9] as follows:

$$\int_{ab} (\rho u_n u_x + p_\infty)\,\mathrm{d}s + \int_{bc} p_x\,\mathrm{d}s = \int_{cd} (\rho u_n u_x + p_x)\,\mathrm{d}s \tag{10}$$

where ρ, U_x, and p_x are density, velocity, and pressure along the direction of the fuselage length, respectively. U_n is velocity normal to

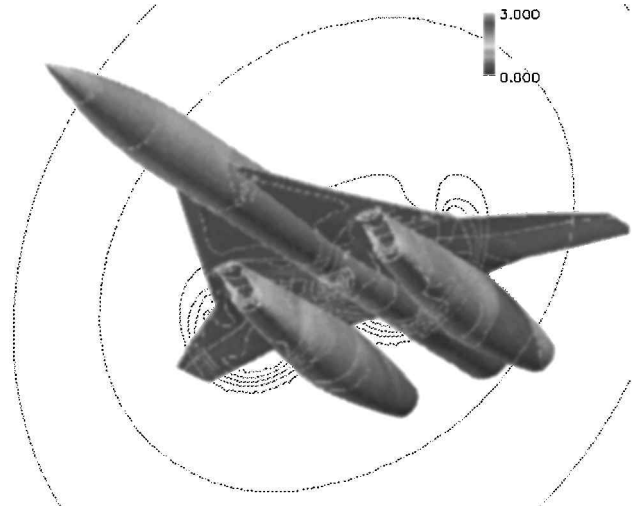

Without throat

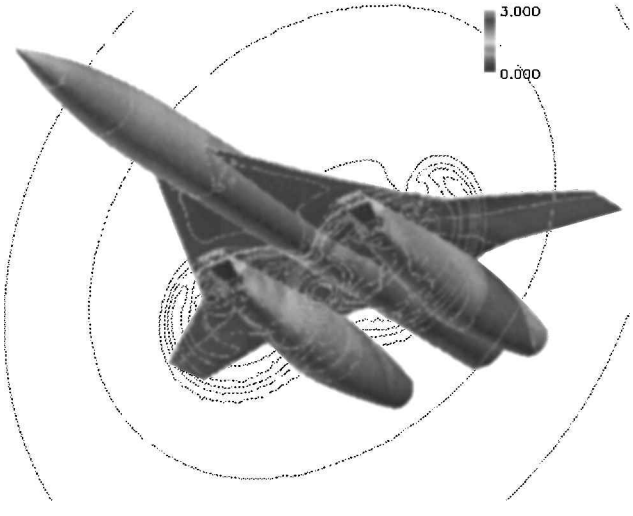

With throat

Fig. 7 Computed surface pressure and pressure contours at crossflow plane of the wing–body–nacelle configuration.

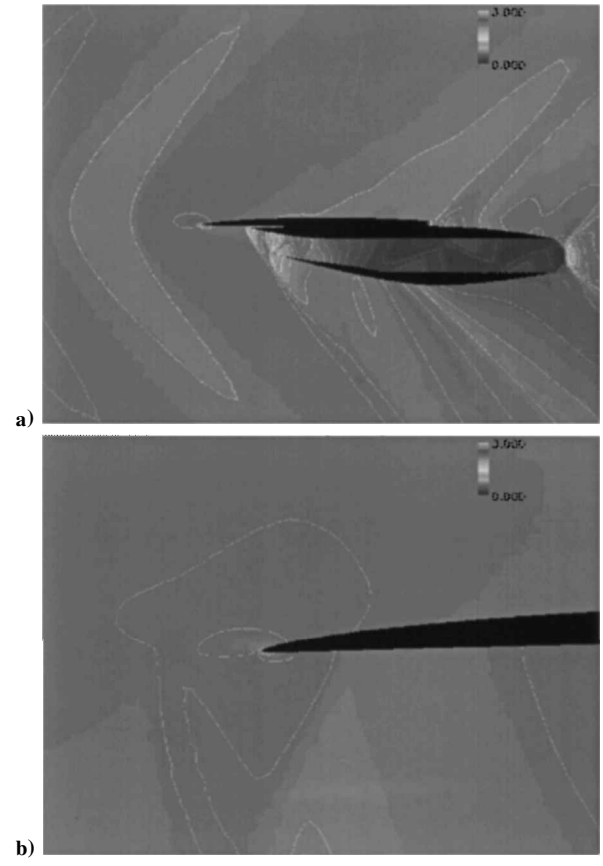

Fig. 8 Computed pressure contours along a cross-sectional view of the nacelle and outer wing without throat: a) 33% semispan length and b) close-up view of the leading-edge region at 50% span-span length.

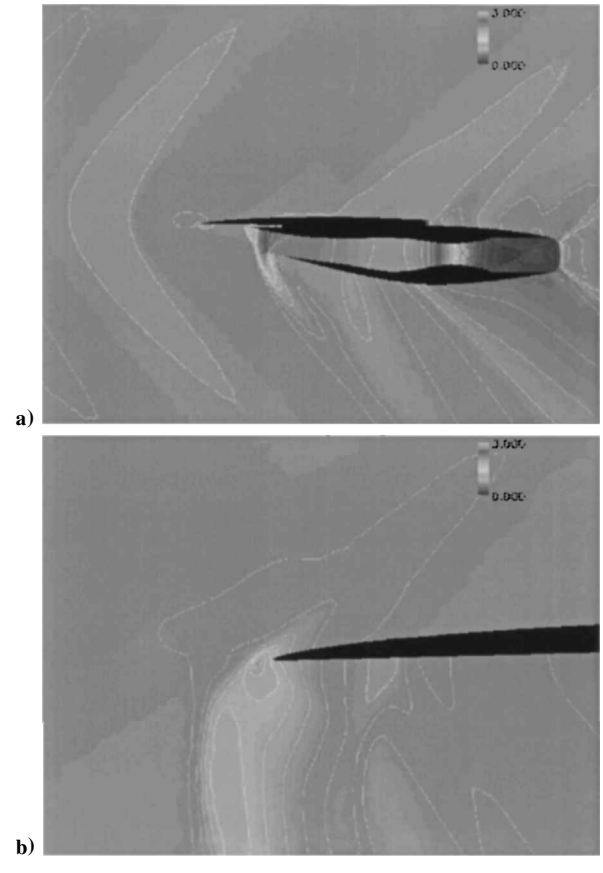

Fig. 9 Computed pressure contours along a cross-sectional view of the nacelle and outer wing with throat: a) 33% semispan length and b) close-up view of the leading-edge region at 50% span-span length.

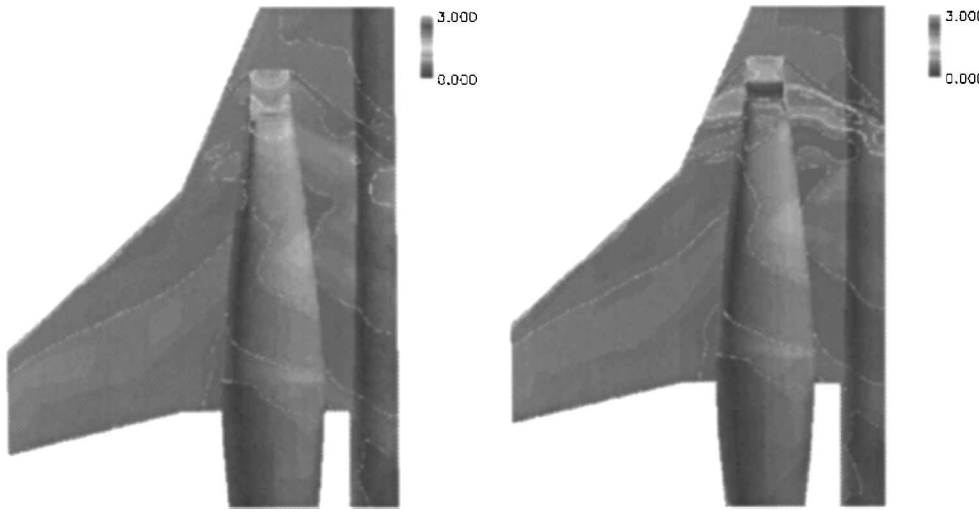

Without throat **With throat**

Fig. 10 Computed pressure contours along the lower surface of the model.

the boundary, and p_∞ is freestream pressure. Hence, the equilibrium of forces is written as

$$\int_{ab} p_\infty \, ds + \int_{bc} p_\infty \, ds = \int_{cd} p_\infty \, ds \tag{11}$$

Equations (10) and (11) give the equation written as

$$\int_{ab} \rho u_n u_x \, ds + \int_{bc} (p_x - p_\infty) \, ds = \int_{cd} [\rho u_n u_x + (p_x - p_\infty)] \, ds \tag{12}$$

The second term

$$\int_{bc} (p_x - p_\infty) \, ds$$

corresponds to the spillage drag, and ρu_n corresponds to the mass flow through a unit area normal to the boundary. It is still difficult to calculate the first integration

$$\int_{ab} \rho u_n u_x \, ds$$

because the point b has to be determined from the streamline that will reach the point c at every mass flow ratio, as illustrated in Fig. 4. Considering the conservation of the mass flow, one can obtain the relation written as

$$\int_{ab} \rho u_n u_x \, ds = u_\infty \int_{ab} \rho u_n \, ds = u_\infty \int_{cd} \rho u_n \, ds \tag{13}$$

By the use of this equation, the spillage drag is rewritten as

$$D_{\text{spil}} = \int_{cd} [\rho u_x (u_x - u_\infty) + (p - p_\infty)] \, ds \tag{14}$$

Results

The geometry used in the present study is the preliminary wind-tunnel model for the scaled experimental supersonic airplane designed at NAL. The computational grid is shown in Fig. 5. The total numbers of the nodes and elements are about 1,800,000 and 10,000,000, respectively. Solutions were obtained at a freestream Mach number $M_\infty = 1.4$ and an angle of attack of 0 deg. The calculation time was about 720 h using a single CPU of the ORIGIN2000 per case.

Mass Flow Ratio

The mass flow ratio A_0/A_i can be controlled by changing the height of the throat as shown in Fig. 6. In this study, the heights of throat shape were set to 0, 24, 32, 34, and 36% of the nacelle outlet radius. The referenced nacelle radius is 3% of the fuselage length.

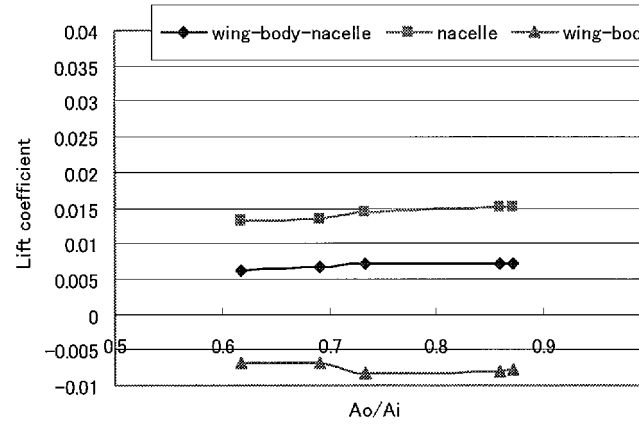

Fig. 11 Variation of lift coefficients vs nacelle mass flow ratios.

Computed Pressure Distributions

Computed pressure contours on the wing–body–nacelle configuration with the 36% height of throat case are compared with the flow-through nacelle case in Fig. 7. Strong shock waves can be found near the nacelle intake with the 36% height of throat shape case. The shock waves extend to the upper surface of the wing (Figs. 8–10).

Effects of the throat on the pressure distributions are also illustrated in Figs. 8–10. Figures 8 and 9 show the computed pressure contours along cross-sectional view of the nacelle. Figure 10 shows the pressure distributions on the lower surface of the model. Whereas the air is not compressed in the flow-through nacelle, the air is highly compressed in the simulated powered nacelle with the throat, as expected. In the latter case, the resulting subsonic region extends upstream of the inlet, and it creates the strong shock wave.

Variations in Aerodynamic Performance Due to Nacelle Mass Flow Ratios

Force measurements in the experiment were processed to exclude aerodynamic forces inside the nacelle. This is because the preliminary estimate of the airplane performance is carried out as a sum of external aerodynamic force and propulsion-related force estimated separately. Following the experiment, the computed lift and drag also excludes forces inside the nacelle.

Lift and drag coefficients at various nacelle mass flow ratios are plotted in Figs. 11 and 12, respectively. In Fig. 11, the lift coefficient of the wing–body increases as the mass flow ratio decreases. This increase was caused by the shock wave near the intake of the nacelle as shown in Fig. 10. On the other hand, the lift coefficient of the nacelle decreases with decreasing mass flow ratio. Figure 12 shows the predicted pressure drag variation as mass flow changes. As the nacelle mass flow ratio decreases, each drag coefficient decreases slightly.

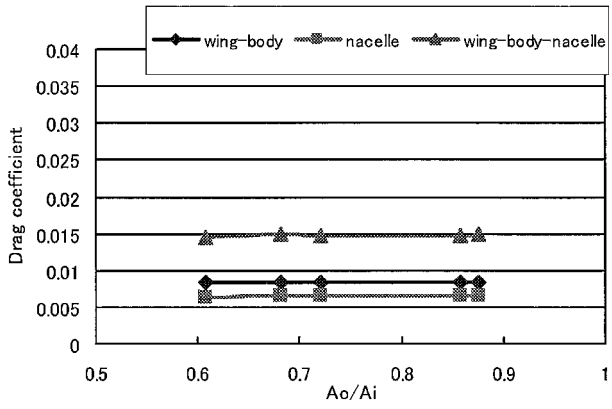

Fig. 12 Variation of predicted pressure drag coefficients vs nacelle mass flow ratios.

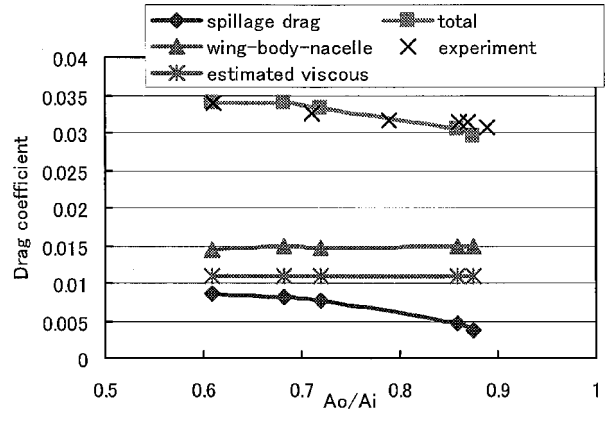

Fig. 13 Comparison of computational results with experiment; total includes predict pressure drag, calculated spillage drag, and estimate viscous drag.

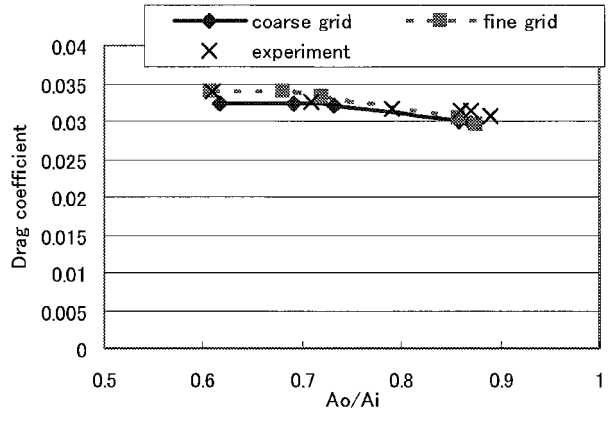

Fig. 14 Comparison of total drag obtained by fine grids and coarse grids.

Does the total drag decrease as the throat reduces the nacelle mass flow ratio, although the strong shock wave appears? It sounds inconsistent because it is. Total drag includes calculated spillage drag and estimated viscous drag,[10] in addition to the predicted pressure drag on the wing–body–nacelle. This leads to the calculation of the spillage drag estimated from Eq. (14). Figure 13 shows the spillage drag and the total drag coefficients compared with experiment. The spillage drag does increase as the nacelle mass flow ratio decreases.

In the design process of the supersonic transport model by NAL, the viscous drag is estimated from the wetted area and turbulent boundary-layer approximation. Thus far, NAL does not find strong viscous interactions, and, thus, the viscous drag estimation is considered valid. Therefore, the viscous drag was also estimated using the same method in this study. When the estimated viscous drag is added to the external pressure drag obtained from the present inviscid computations, the total drag shows excellent agreement with experimental data.

Grid Resolution Study

To investigate the grid dependency on the numerical solution, coarse grids were also used. The total numbers of nodes and elements of the coarse grids are about 910,000 and 5,100,000, respectively, which are roughly one-half of the numbers on the fine grid used for the results shown earlier.

Figure 14 shows a comparison of the total drag coefficients between coarse and fine grids. According to Fig. 14, both cases are identical at the high mass flow ratio. Although both cases are agree reasonably well at the low mass flow ratio, the total drag calculated by the fine grid shows better agreement with experimental data than that of the coarse grid. These results show that the present fine grid has reasonable resolution.

Conclusions

The numerical simulation of supersonic flows around the wing–body–nacelle configuration of the NAL scaled supersonic experimental airplane has been performed at various nacelle mass flow ratios by changing the throat heights inside the nacelle. In this study, flowfields were simulated by solving the Euler equations with the unstructured grid method.

The external pressure drag was found to decrease as the nacelle mass flow ratio decreased, whereas the shock wave moved upstream and finally moved out from the inlet. The spillage drag was calculated and found to increase as the nacelle mass flow ratio decreased. Because of the spillage drag, the total drag is confirmed to increase as the nacelle mass flow ratio decreases. The computed drag agrees well with wind-tunnel data obtained at NAL when the viscous drag estimation is included.

The grid dependency of the numerical solution was investigated using coarse grids, and it was verified that the present fine grid has reasonable resolution.

Acknowledgments

We thank the National Aerospace Laboratory of Japan supersonic experimental aircraft project team for providing the original geometry and its wind-tunnel measurements. The calculations were performed using the supercomputer ORIGIN2000 in the Institute of Fluid Science, Tohoku University.

References

[1]Shimbo, Y., Yoshida, K., Iwamiya, T., and Matsushima, K., "Aerodynamic Design of Scaled Supersonic Experimental Airplane," 1998, pp. 62–67.

[2]Sharov, D., and Nakahashi, K., "Reordering of Three-Dimensional Hybrid Unstructured Grids for Lower–Upper Symmetric Gauss–Seidel Computations," *AIAA Journal*, Vol. 36, No. 3, 1998, pp. 484–486.

[3]Fujita, T., Ito, Y., Nakahashi, K., and Iwamiya, T., "Aerodynamics Evaluation of NAL Experimental Supersonic Airplane in Ascent Using CFD," AIAA Paper 2001-0564, Jan. 2001.

[4]Ito, Y., and Nakahashi, K., "Direct Surface Triangulation Using Stereolithography (STL) Data," AIAA Paper 2000-0924, 2000.

[5]Sharov, D., and Nakahashi, K., "Hybrid Prismatic/Tetrahedral Grid Generation for Viscous Flow Applications," *AIAA Journal*, Vol. 36, No. 2, 1998, pp. 157–162.

[6]Shimbo, Y., Makino, Y., and Noguchi, M., "Wind Tunnel Test of the Powered National Supersonic Experimental Transport," *48th Annual Meeting of the Japan Society of Fluid Mechanics*, 2001, pp. 84–93 (in Japanese).

[7]Obayashi, S., and Guruswamy, G. P., "Convergence Acceleration of an Aeroelastic Navier–Stokes Solver," *AIAA Journal*, Vol. 33, No. 6, 1995, pp. 1134–1141.

[8]Venkatakrishnan, V., "On the Accuracy of Limiters and Convergence to Steady State Solutions," AIAA Paper 93-0880, 1993.

[9]Jameson, A., and Turkel, E., "Implicit Schemes and LU Decompositions," *Mathematics of Computation*, Vol. 37, No. 156, 1981, pp. 385–397.

[10]Yoshida, Y., Noguchi, M., Shimbo, Y., and Kuroda, F., "Comparison of Wind Tunnel Test and CFD Analysis on an Airframe/Nacelle Configuration of the Scaled Supersonic Experimental Airplane," *39th Aircraft Symposium* [CD-ROM], 2001 (in Japanese).

P. Givi
Associate Editor